

Deep Learning-Based Impurity Evaluation: Targeting Silicon Solar Cells' Photovoltaic Parameters

Oleg Olikh
Physics Faculty
Taras Shevchenko National
University of Kyiv
Kyiv, Ukraine
olegolikh@knu.ua

Oleksii Zavhorodnii
Physics Faculty
Taras Shevchenko National
University of Kyiv
Kyiv, Ukraine
nevermor464@gmail.com

Yaroslav Olikh
Kinetic Phenomena and Polaritonics
Department
V.E. Lashkaryov Institute of
Semiconductor Physics of National
Academy of Sciences of Ukraine
Kyiv, Ukraine
jaroluk3@ukr.net

Svitlana Gapochenko
Physics Department
National Technical University
"Kharkiv Polytechnic Institute"
Kharkiv, Ukraine
svitlana.gapochenko@khp.edu.ua

Olena Lyubchenko
Physics Department
National Technical University
"Kharkiv Polytechnic Institute"
Kharkiv, Ukraine
olena.lyubchenko@khp.edu.ua

Abstract — In our work, we applied the deep learning-based approach for estimating an iron concentration in silicon solar cells by using photovoltaic parameters. Different variants of deep neural networks, which involve using either the short-circuit current, photoconversion efficiency, open-circuit voltage, and fill factor values, or only the first two parameters obtained under solar or monochromatic lighting, were examined. The simulation of silicon solar cells for generating labeled datasets was performed using SCAPS-1D software. Networks were tested on synthetic and experimental current-voltage characteristics. It was shown that the mean-squared error of iron concentration predictions can be about 3×10^{-3} . The ways of

optimizing the configuration and use of such neural networks are proposed.

Keywords — silicon solar cell, iron contamination, deep neural network, photovoltaic parameters, SCAPS, recombination centers

I. INTRODUCTION

Materials informatics (MI), which combines material property calculations/measurements and informatics algorithms, has become one of the main paradigms of science over the past few years [1]. MI has opened new avenues for accelerating the development, characterization, and investigation of both materials and devices. At the same time, one of the most important directions is the use of machine learning methods, which are focused on solving problems where the possibility of clear algorithm presentation is not foreseen. In particular, similar approaches are widely used in photovoltaics, which occupies a special place among technologies of renewable energy sources. For example, computer-assisted learning is used to identify potentially important photovoltaic materials based on their optical and symmetry properties [2] or the mentions of the various structure names in the literature [3], to predict solar cell current-voltage characteristics (IVC) [4] and their degradation [5] depending on external conditions, and to automate of defect detection procedures based on electroluminescent images [6].

On the other hand, non-destructive methods aimed at estimating the concentration of recombination-active defects, in particular, the impurities, in photovoltaic semiconductor structures are important from an applied point. Today, many

direct and indirect methods have been developed to solve this problem. The improvement of methods is often achieved not only by using more advanced experimental procedures and equipment but also due to various mathematical tools. Laplace deep-level transient spectroscopy (LDLTS) [7] may be considered as the most striking example. In this case, the Laplace transforms allowed not only to simplify the experimental procedure compared to classical DLTS (when there are enough measurements at a single temperature) but also a significant increase in the resolution of defects' energy determination.

However, almost all existing methods require special preparation of the research objects or special equipment. At the same time, a simple and generally accepted method of determining the parameters of the photovoltaic conversion of solar cells is the measurement of IVC. Obviously, the presence of recombination centers significantly affects the processes of photoelectric conversion. That means the determination of the characteristics of such defects precisely from the analysis of IVC is both fundamentally possible [8] – [9] and extremely promising for wide use. Obviously, the mathematical tools for IVC processing are perhaps the most important in that case. For example, it was proposed to use differential I-V coefficients [10] and current components [9] for defect characterization. Moreover, the extraction of the current components from measured IV curves is improved by using the Lambert W-function [11]. Lately, the ability to extract the defect parameters from IV measurements and Bayesian parameter estimation utilizing a modified Gaussian likelihood was demonstrated [12]. However, one of the most considerable obstacles to introducing such a convenient and quick method remains the multi-parameter nature of the analytical interrelationship of the recombination center concentration and the IVC features. And it is the use of deep learning methods that can be a way to overcome this obstacle.

In particular, it is about the creation of an artificial deep neural network (DNN), which can predict the concentration of electrically active impurities, using the base general characteristics of a solar cell (SC), measurement conditions, and certain parameters of IVC. Of course, DNN training requires a huge amount of labeled data, and the first step to obtain such data can be the SC simulation using standard

software. The possibility of implementing a similar approach was shown in our previous work [13], where the dark IVCs were studied, and the ideality factor was considered as the parameter which was essentially sensitive to the influence of recombination centers. This paper presents the results of constructing a DNN that uses standard photovoltaic parameters: short-circuit current (I_{SC}), open-circuit voltage (V_{OC}), efficiency (η), and fill factor (FF). This approach makes it possible to reduce the requirements for IVC measurement. In addition, the measurement of light IVC is a more common way of SCs characterization. The choice of monocrystalline silicon photoconverters as a research object is determined by the predominant practical application of such structures. In turn, iron is one of the main and most harmful impurities in such systems, which led to using the DNN for the detection of such recombination centers.

II. SIMULATION DETAILS AND DNN MODELS

The $n^+ - p - p^+$ structure was under consideration. Such back surface field (BSF) configuration is one of the popular designs that have been used in the mass-production of c -Si SCs [14]. The thicknesses of the uniformly doped n^+ emitter, p base, and p^+ layer were assumed to be d_n , d_p , and d_{BSF} , respectively, and the dopant concentrations (phosphorus or boron) in these layers were N_D , N_B , and N_{BSF} . To create the labeled datasets, the IVCs of the specified structures were simulated at different temperatures T and lighting conditions using the SCAPS 3.3.10 software package [15] and I_{SC} , V_{OC} , η and FF were determined. In a simulation, it was supposed that the cause of Shockley-Read-Hall recombination is an impurity iron, which is homogeneously distributed with the N_{Fe} concentration in the regions with hole conductivity. Intrinsic recombination and recombination on the outer structure surfaces were also taken into account. Temperature dependences of silicon parameters (gap width, gap narrowing due to doping, intrinsic recombination coefficients, carrier mobilities, etc.) and recombination centers were also considered. Two defect configurations were examined: i) all impurity iron atoms were in the interstitial positions, ii) some of them formed pairs with the acceptor, at that, the ratio of Fe_i and FeB concentrations depends on the Fermi level location at a certain point of the structure. In practice, the first case can be realized by intense SC light exposition or high-temperature treatment (210°C, 3 min) [16], and the second one corresponds to an equilibrium state. Details of simulating features are given in [13].

The parameter values used in the simulation are shown in Table 1. Note that the selected light exposition conditions correspond to standard SC testing conditions (solar spectrum AM1.5) and the case of low-intensity monochromatic light exposition, for example, using the SN-HPIR940nm-1W LED. The second mode is convenient for the photoinduced process analysis, as it corresponds to the generation of nonequilibrium carriers in the depth of the base outside the region of space charge. When preparing the training labeled dataset, 5 d_p values, 9 N_B values, 11 T values, and 25 N_{Fe} values, which were uniformly distributed (thickness and temperature in a linear scale, concentrations - in logarithmic scale) over the ranges specified in Table 1, were used for each configuration of defects and each exposition mode. Thus,

24,750 IVCs were prepared to create a training set for the cases of both white and monochromatic light exposition. Several test datasets whose names reflect the simulation features were also created. For example, during the Fe -varied dataset preparation, the IVC simulation was carried out using the d_p , N_B , and T , which were used in the training set preparation, while the iron concentrations were chosen differently. This set was based on 1,806 IVCs for monochromatic light exposition and 2,252 ones for AM1.5. The B -varied set (2,202 IVCs for each exposition case) provided the use of doping levels different from the training set; the All-varied set was based on 14,704 IVCs of the structures, in which simulation the values of all four variable parameters differed from those used earlier.

TABLE I. THE PARAMETERS VALUES USED IN THE SIMULATION

Parameter	Values
d_n , μm	0.5
d_p , μm	180 – 380
d_{BSF} , μm	1
N_D , cm^{-3}	10^{19}
N_B , cm^{-3}	$10^{15} - 10^{17}$
N_{BSF} , cm^{-3}	5×10^{18}
N_{Fe} , cm^{-3}	$10^{15} - 10^{17}$
T , K	290 – 340
Light exposition	AM1.5, 1000 W/m ² ; 940 nm, 4 W/m ²

Note that the existence of only one type of recombination center is unlikely in a real situation. Therefore, to separate the impact of the defects associated with iron on the photoelectric parameters, the relative changes of each of them were used:

$$\varepsilon A = \Delta A / A_{FeB} \times 100\% = (A_{FeB} - A_{Fe}) \times 100\%, \quad (1)$$

where A is the SC parameter (I_{SC} , V_{OC} , FF , and η), the index "FeB" corresponds to the value of the parameter in the case of coexistence of Fe_i and FeB , the index "Fe" is related to the decay of all pairs.

The dense DNN was implemented through a high-level Keras API provided by TensorFlow. For each light exposition mode, two variants of fully connected DNNs, which differed in the number of input nodes, were considered. In the first version of DNN, the input layer consisted of 5 nodes, on which the standard normalized values of d_p and $\lg N_B$ (SC parameters), T (external environment), εI_{SC} and $\varepsilon \eta$ (IVC characteristics) were supplied. A network that used the values obtained under white light exposition is denoted as DNN_{AM,5}; and a network that used values obtained at monochromatic light exposition – as DNN_{λ,5}. In the second version of DNN, the input layer contained two additional nodes, which values were determined by εV_{OC} and εFF . The corresponding networks are denoted as DNN_{AM,7} and DNN_{λ,7}. The choice of such configurations of input nodes was due to the fact that the short-circuit current and efficiency are the most sensitive to changes in iron concentration [17].

The output layer of all DNNs contained one node, used a linear activation function, and predicted the logarithm of iron concentration. The mean squared error (MSE) was used as the loss function.

During the network setting, various configurations of hidden layers were considered and rational values of such hyperparameters as the batch size (BS), the activation function (ActF), the optimizer (Opt), the learning rate (LR), the epochs number (N_{ep}), the preprocessing method (PreM), the weight initializer (WI), the regularization function were chosen. In particular, 5 variants of hidden layers (see Fig. 1) with different numbers of nodes in the first layer (N_{nl}) and layers (N_{hl}) were studied.

The training dataset was used for setting, and a random search was performed using the Keras Tuner package. It turned out that the use of regularization is impractical for all networks, and the rational method of preliminary data preparation is StandartScaler. The optimal parameter values are summarized in Table 2.

After the network optimization, their teaching on the training set and verification of predictive properties on the test sets were carried out. It is known that increasing the labeled dataset used for training should improve the performance of DNNs. Therefore, each network was also trained on the so-called full dataset, which consisted of the training and all test datasets. The trained networks were also applied to the IVC measurement results of real SCs.

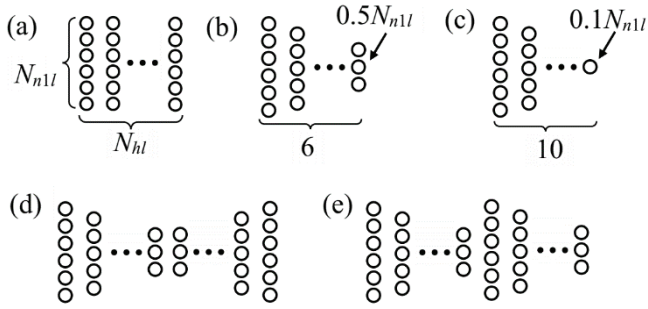


Fig. 1. The considered configuration of the hidden layers: a) pipe; b) trapezium; c) triangle; d) butterfly (two serial reflected trapezium); e) fir (two serial trapezium).

TABLE II. CHOSEN HYPERPARAMETER COMBINATIONS

	DNN _{AM,5}	DNN _{AM,7}	DNN _{Δ,5}	DNN _{Δ,7}
Hidden layers configuration	180-180-180-180-180-180-180-180	200-200-200-200-200-200-200-200	150-150-150-150-150-150-150-150	100-90-80-70-60-50-100-90-80-70-60-50
BS	64	64	64	32
ActF	Elu	Elu	Selu	Selu
Opt	Adam	Nadam	Adam	Nadam
LR	2×10^{-4}	3×10^{-4}	1.5×10^{-4}	6.6×10^{-4}
Nep	600	1500	1200	300
WI	Xavier Normal	Xavier Normal	Random Normal	Random Normal

The calculation was processed in a PC with the following features: AMD Ryzen 5 3600 6-Core Processor 3.59 GHz CPU, 16 GB RAM, GPU NVIDIA GeForce GTX 1650 GDDR5 4096 MB, Windows 10 OS, and Anaconda 3 distribution. The times required to train the DNNs were about 6 min and 7.5 min for the full and training datasets, respectively. Accordingly, the hyperparameters tuning for each network took ~ 140 hours of calculation time. The

prediction time of the trained network is less than 0.5 seconds.

III. RESULTS AND DISCUSSION

A 5-fold cross-validation was used to quantify the predictive properties of the DNN on the training set. The results are presented in Table 3. Relative changes in short-circuit current and efficiency due to recombination on iron-containing defects are significantly larger than the relative changes in open-circuit voltages and form factor: the results of our simulations and [17] shows that at $T = 300$ K and $N_{Fe} \approx 10^{12} \text{ cm}^{-3}$, εI_{SC} and $\varepsilon \eta$ are about 10%, while $\varepsilon V_{OS} \approx 2\%$, and $\varepsilon FF \approx 0.5\%$. However, it can be seen from Table 3 that the additional use of information about V_{OC} and FF during DNN setting increases the degree of training. This is especially noticeable for a network oriented on IVCs obtained under the wide-spectrum light exposition: the difference between the MSEs for DNN_{AM,7} and DNN_{AM,5} reaches three orders of magnitude. For monochromatic light with 940 nm-wavelength [18]:

$$I_{SC} \sim \alpha L / (1 + \alpha L), \quad (2)$$

where α is the coefficient of light absorption, L is the base minority carrier diffusion lengths, which is uniquely related to iron concentration [19]:

$$N_{Fe} = 1.05 \times 10^{16} (L_1^{-2} - L_0^{-2}), \quad (3)$$

where L_0 and L_1 are the diffusion lengths before and after FeB pair dissociation, respectively. That is in this case, the relationship between the impurity concentration and the IVC parameters of the SC is not too complicated, and the DNN with a small number of input nodes is able to track it. Additional input values do not lead to a significant increase in the quality of network fitting to labeled data (MSE change is about 25%), but they expedite the learning process itself (see data for N_{ep} in Table 2).

TABLE III. RESULTS OF 5-FOLD CROSS-VALIDATION

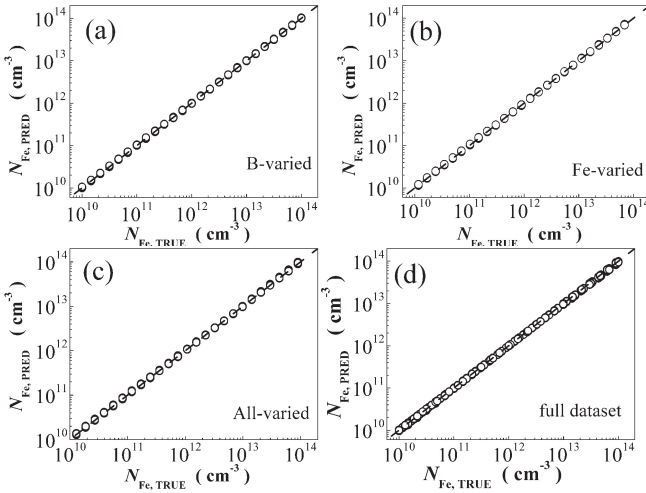
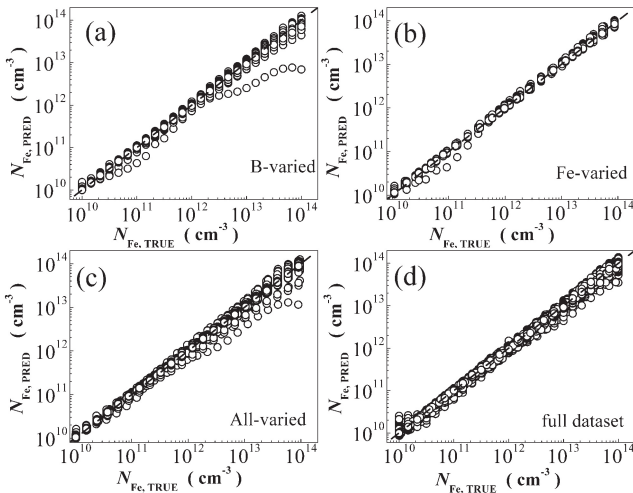
Dataset	MSE			
	DNN _{AM,5}	DNN _{AM,7}	DNN _{Δ,5}	DNN _{Δ,7}
Training	0.04 ± 0.02	$(4 \pm 2) \times 10^{-5}$	$(2.9 \pm 0.8) \times 10^{-3}$	$(2.2 \pm 0.8) \times 10^{-3}$
Full	$(3.7 \pm 0.8) \times 10^{-3}$	$(5 \pm 2) \times 10^{-5}$	$(2.2 \pm 0.8) \times 10^{-3}$	$(1.5 \pm 0.3) \times 10^{-3}$

The trained networks were applied for predictions on synthetic test datasets. To assess the quality of predictions the coefficient of determination R^2 and the Pearson correlation coefficient R between $N_{Fe, \text{TRUE}, i}$ (the iron concentration used in the i -th sample simulation) and $N_{Fe, \text{PRED}, i}$ (the DNN prediction for the i -th sample) were used in addition to MSE. The results are presented in Table 4. In addition, Fig. 2 and 3 show the typical relationships between true and predicted values of iron concentration.

Note that both for the training dataset and for the test datasets, the best results are observed for DNN_{AM,7}, and taking into account of εV_{OC} and εFF increases the prediction accuracy. The level of improvement for the "monochromatic" network can be significantly higher: e.g., MSE decreased by more than by 40% for All-varied set, and by 2.7 times for the B-varied set.

TABLE IV. RESULTS OF DNN ON SYNTHETIC IV CURVES

Network	Parameter	Test dataset		
		B-varied	Fe-varied	All-varied
$DNN_{AM,5}$	MSE	0.013	0.015	0.011
	R^2	0.9912	0.9927	0.9845
	R	0.9956	0.9963	0.9922
$DNN_{AM,7}$	MSE	0.00030	0.00030	0.00051
	R^2	0.9998	0.9997	0.9990
	R	0.999	0.9999	0.9995
$DNN_{\lambda,5}$	MSE	0.52	0.009	0.019
	R^2	0.9350	0.9874	0.9611
	R	0.9670	0.9934	0.9804
$DNN_{\lambda,7}$	MSE	0.019	0.009	0.011
	R^2	0.9652	0.9785	0.9638
	R	0.9825	0.9892	0.9818

Fig. 2. Iron concentrations are plotted against those generated by $DNN_{AM,7}$ on B-varied (a), Fe-varied (b), All-varied (c), and full (F) datasets. The black dashed lines are the identify lines serving as the references.Fig. 3. Iron concentrations are plotted against those generated by $DNN_{\lambda,5}$ on B-varied (a), Fe-varied (b), All-varied (c), and full (F) datasets. The black dashed lines are the identify lines serving as the references.

Despite the fact that the $DNN_{AM,5}$ training results were worse than for both DNN_{λ} networks, its predictions when working with unfamiliar data were better in most cases. It is also interesting that when the network is faced with unfamiliar doping level values, the predictive performance is even worse than when working with samples for which d_p , N_B and T values were not used during training. This indicates the importance of training such networks using the doping concentrations that are expected in further evaluation activities. A similar feature was discovered earlier in the development of networks that use the imperfection factor for iron concentration evaluation [13]. The reason is a decisive impact of the doping degree on the Fermi level position, and as a result on the ratio of concentrations of various iron-containing defects.

On the other hand, the Fe-varied set is probably the closest to the real situation, which involves the possibility of training the network for structures with well-defined parameters and IVCs measured under standard conditions. As the obtained results show, all considered networks are very effective in estimating an iron concentration deviation from standard values. In particular, the values of the coefficients of determination and correlation are close to 0.99 for the Fe-varied test set.

Increasing the number of values in the dataset for the network training (using the full dataset instead of the training dataset during training, see Table 3, Fig. 2d, and Fig. 3d) significantly improves the predictive properties only for $DNN_{AM,5}$, i.e., the network with the worst performance for the training dataset. For $DNN_{\lambda,7}$ and $DNN_{\lambda,5}$, the MSE reduction is commensurate with the error, and was not detected for $DNN_{AM,7}$ at all.

The ability of DNNs to predict an iron concentration in real silicon SCs was tested as well. The samples used in the experiment were $n^+ - p - p^+ - Si$ structures fabricated from p -type boron doped Czochralski silicon wafer with [100] orientation and the resistivity of $10 \Omega \cdot cm$ ($N_B = 1.4 \cdot 10^{15} cm^{-3}$). The n^+ emitter with a sheet resistance of about $20 - 30 \Omega/m^2$ and $0.7 \mu m$ thickness was formed by phosphorus diffusion at 1215 K; and p^+ layer ($10 - 20 \Omega/m^2$; $0.6 \mu m$) was formed by boron diffusion at 1260 K. The base thickness was $350 \mu m$. The area of the samples was $1.52 \times 1.535 cm^2$. The concentration of iron in the SC base $N_{Fe,MEAS}$ was determined from the kinetics of the short circuit current under monochromatic light exposition [20]. Four samples with $N_{Fe,MEAS}$ equal to $(2.0 \pm 0.4) \cdot 10^{12}$, $(6.7 \pm 0.7) \cdot 10^{12}$, $(9.8 \pm 0.9) \cdot 10^{12}$, and $(1.9 \pm 0.4) \cdot 10^{13} cm^{-3}$ were used. IVC measurements were carried out at 300, 320, and 340 K, under illumination using a light-emitting diode SN-HPIR940nm-1W, which maximum emissive ability corresponded to 940 nm. The illumination power, measured with a PowerMeter Rk-5720, was about $30 \mu W/cm^2$. The decomposition of FeB pairs was initiated by a halogen lamp light exposition. The approach proposed in [21] was used to determine the photoelectric conversion parameters from the IVC type. The results of using the $DNN_{\lambda,5}$ and $DNN_{\lambda,7}$ networks, trained on the training set or on the full set, are presented in Fig. 4.

The results obtained for experimental IVC curves are generally worse than for synthetic ones. However, common features can be identified for these cases. Namely, increasing the input node number improves the prediction quality (this follows from comparison of Fig. 4a and Fig. 4b). The decrease in errors for networks trained on all simulated data (the half-filled points in Fig. 4 are in most cases closer to the dotted line than the unfilled ones) may be due both to the usual increase in the labeled dataset (see Table 3) and to the absence in the training set of the samples with a value of $N_B = 1.4 \cdot 10^{15} \text{ cm}^{-3}$ as opposed to the full set. That is, the experimental data are somewhat similar both to the B-varied (or All-varied) testing set for networks trained using the training set and to the Fe-varied set for DNNs trained with the full set.

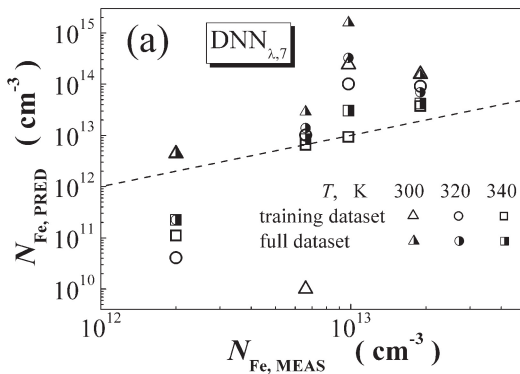


Fig. 4. Results of applying the $\text{DNN}_{\lambda,7}$ (a) and $\text{DNN}_{\lambda,5}$ (b) networks, previously trained on the training (empty dots) or full (half-filled dots) sets, to the experimental IVCs. The dashed lines are the identifying lines serving as the references.

Given the successes of networks on synthetic data, we believe that improving the DNNs performance on experimental data can be achieved by applying a more perfect computational model to obtain labeled data. In particular, it is advisable to take into account the real profile of ligands in the emitter and BSF-layer obtained from diffusion [22] and the dependencies of surface recombination speeds on boron and phosphorus concentrations [23]. Another way is a model training on the array of real solar cells of a certain type with certified impurity content data. This approach may be appropriate under industrial production conditions.

IV. CONCLUSION

For the first time, the deep neural networks to predict the concentration of impurity iron in silicon $n^+ - p - p^+$ structures using the values of base doping level and thickness, temperature, and relative changes in photovoltaic parameters after the dissociation of FeB pairs have been designed and configured. It is shown by using simulated data that under solar light exposition, the use of open-circuit voltage and form factor in the input layer in addition to short-circuit current and efficiency provides increasing the accuracy of network predictions by 2-3 orders. At the monochromatic light exposition that corresponds to the uniform photogeneration of charge carriers in the volume of solar element, additional input values improve the prognostic properties by only 20-30% but give a possibility of increase in learning training speed. It is shown that the highest accuracy of iron concentration estimations is observed for structures with a doping level that corresponds to the values

used during network training. At the same time, DNNs can determine the concentration values of impurities that were not used during training, with sufficiently high accuracy. Neural networks trained on synthetic data were tested on real solar cells. Possible ways of improving the evaluation accuracy due to the modification of the calculation model to obtain a labeled dataset were considered.

REFERENCES

- [1] S. Ju, S. Shimizu, and J. Shiomi, "Designing thermal functional materials by coupling thermal transport calculations and machine learning", *J Appl. Phys.*, vol. 128 (16), 161102, October 2020.
- [2] H.-J. Feng and P. Ma, "Machine learning prediction of 2D perovskite photovoltaics and interaction with energetic ion implantation", *Appl. Phys. Lett.*, vol. 119 (23), 231902, December 2021.
- [3] L. Zhang and M. He, "Unsupervised machine learning for solar cell materials from the literature", *J Appl. Phys.*, vol. 131 (6), 064902, February 2022.
- [4] T. Guzel and A.B. Colak, "Artificial intelligence approach on predicting current values of polymer interface Schottky diode based on temperature and voltage: An experimental study", *Superlattices and Microstructures*, vol. 153, 106864, May 2021.
- [5] T.W. David, G.A. Soares, N. Bristow, D. Bagnis, and J. Kettle, "Predicting diurnal outdoor performance and degradation of organic photovoltaics via machine learning; relating degradation to outdoor stress conditions", *Prog. Photovolt. Res. Appl.*, vol.29 (12), pp. 1274-1284, December 2021.
- [6] Y. Zhao, K. Zhan, Z. Wang, and W. Shen "Deep learning-based automatic detection of multitype defects in photovoltaic modules and application in real production line", *Prog. Photovolt. Res. Appl.*, vol.29 (4), pp. 471-484, April 2021.
- [7] L. Dobaczewski, A.R. Peaker, K.B. Nielsen, "Laplace-transform deep-level spectroscopy: The technique and its applications to the study of point defects in semiconductors", *J Appl. Phys.*, vol. 96 (9), pp. 4689-4728, December 2004.
- [8] O. Olikh, "Relationship between the ideality factor and the iron concentration in silicon solar cells", *Superlattices and Microstructures*, vol. 136, 106309, December 2019.
- [9] C. Claeys and E. Simoen, "Device performance as a metrology tool to detect metals in silicon", *Phys. Status Solidi (a)*, vol. 216 (17), 1900126, September 2019.
- [10] S.V. Bulyarskiy, A.V. Lakalin, M.A. Saurov, and G.G. Gusarov "The effect of vacancy-impurity complexes in silicon on the current-voltage characteristics of p-n junctions", *J Appl. Phys.*, vol. 128 (15), 155702, October 2020.
- [11] X. Gao, Y. Cui, J. Hu et al., "Lambert W-function based exact representation for double diode model of solar cells: Comparison on fitness and parameter extraction", *Energy Conversion and Management*, vol. 127, pp. 443-460, November 2016.
- [12] R.C. Kurchin, J.R. Poindexter, V. Vahanissi et al., "How much physics is in a current-voltage curve? Inferring defect properties from photovoltaic device measurements", *IEEE Journal Of Photovoltaics*, vol.10 (6), pp. 1532-1537, November 2020.
- [13] O. Olikh, O. Lozitsky, and O. Zavorodnii, "Estimation for iron contamination in Si solar cell by ideality factor: Deep neural network approach", *Prog. Photovolt. Res. Appl.*, vol.30 (6), pp. 648-660, June 2022.
- [14] M.A. Green, "Photovoltaic technology and visions for the future", *Prog. Energy*, vol. 1 (1), 13001, July 2019.
- [15] M. Burgelman, P. Nollet and S. Degraeve, "Modelling polycrystalline semiconductor solar cells", *Thin Solid Films*, vol. 361-362, pp. 527-532, February 2000.
- [16] L.J. Geerlings and D. Macdonald, "Dynamics of light-induced FeB pair dissociation in crystalline silicon", *Appl Phys Lett.*, vol.85 (22), pp. 5227-5229, November 2004.
- [17] M.C. Schubert, M. Padilla, B. Michl et al., "Iron related solar cell instability: Imaging analysis and impact on cell performance", *Sol. Ener. Mat. & Sol. Cells*, vol.138, pp. 96-101, July 2015.
- [18] A. Fahrenbruch and R. Bube, *Fundamentals of Solar Cells: Photovoltaic Solar Energy Conversion*, New York: Academic Press, 1983, p.580.

- [19] G. Zoth and W. Bergholz, "A fast, preparation-free method to detect iron in silicon", *J. Appl. Phys.*, vol. 67 (11), pp. 6764-6771, June 1990.
- [20] O. Olikh, V. Kostilyov, V. Vlasuk et al., "Features of FeB pair light-induced dissociation and repair in silicon n⁺-p-p⁺ structures under ultrasound loading", *J Appl. Phys.*, vol. 130 (23), 235703, December 2021.
- [21] B. Paviet-Salomon, J. Levrat, V. Fakhfour et al., "New guidelines for a more accurate extraction of solar cells and modules key data from their current-voltage curves", *Prog. Photovolt. Res. Appl.*, vol.25 (7), pp. 623-635, July 2017.
- [22] A. Fell, K.R. McIntosh, P.P. Altermatt et al., "Input parameters for the simulation of silicon solar cells in 2014", *IEEE Journal Of Photovoltaics*, vol.5 (4), pp. 1250-1263, July 2015.
- [23] P.P. Altermatt, "Models for numerical device simulations of crystalline silicon solar cells – a review", *J. Comput. Electron.*, vol.10 (6), pp. 314-330, July 2011.